--SUPPORTING INFORMATION--

Analysis of Solid-State Reaction Mechanisms with Two-Dimensional FTIR Correlation Spectroscopy

Nataraju Bodappa,[a] Sarah Stepan,[a] Rodney D. L. Smith[a,b,*]

[a]*Department of Chemistry, University of Waterloo, 200 University Avenue W., Waterloo, Ontario, Canada N2L 3G1*

[b]*Waterloo Institute for Nanotechnology, University of Waterloo, 200 University Avenue W., Waterloo, Ontario, Canada N2L 3G1*

Correspondence to:

rodsmith@uwaterloo.ca

Table S1. FTIR peak vibrational frequencies for asymmetric and symmetric carboxylate stretching frequencies in metal (II/III) 2-ethylhexanoate films, as obtained from the multi-peak fit in figure S8.

Metal ion	ν_s(COO)	ν_{as}(COO)$_{Chelate}$	ν_{as}(COO)$_{Ionic}$	ν_{as}(COO)$_{Bridge}$		ν_{as}(COO)$_{Monodentate}$
Mn^{2+}	1418.4	1521.87	1560	1591.72	-	1687.6
Fe^{3+}	1423.4	1530.62	1552.6	1591.72	1614	1690.5
Co^{2+}	1419.8	1530.7	1548	1590.6	-	1681.9
Ni^{2+}	1409.4	1530.4	1560	1580.99	1614.7	1680.3
Cu^{2+}	1422.7	1501.91	1547	1578.99	-	-
Zn^{2+}	1426.5	1545.0	1563.5	1592.6	1629.72	-

Table S2. FTIR peak vibrational frequencies for the monometallic films determined from cross peak locations in the 2D-COS synchronous plots.

2-ethylhexanoate(film)	ν_{as}(COO) (cm^{-1})	ν_s(COO) (cm^{-1})	Δ (ν_{as}(COO)- ν_s(COO)) (cm^{-1})	**assignment**
Mn^{2+}	1689	1417	272	Monodentate
	1589		172	Bridge
	1562		145	Ionic
	1520		103	Chelate
Fe^{3+}	1686	1423	263	Monodentate
	1589		166	Bridge
	1552		129	Ionic
	1531		108	Chelate
Co^{2+}	1684	1423	261	Monodentate
	1591		168	Bridge

	1548		117	Ionic
	1531		108	Chelate
Ni^{2+}	1680	1402	278	Monodentate
	1618		214	Bridge
	1577		181	Bridge
	1554		152	Ionic
	1531		108	Chelate
Cu^{2+}	1598	1423	175	Bridge
	1578		155	Bridge
	1542		120	Ionic
	1504		81	Chelate
Zn^{2+}	1591	1415	176	Bridge
	1562		147	Ionic
	1539		124	Chelate

Table S3. Ionic radius, electronegativity, and pK_a of aqua ion values for different metal ions.

Metal ion	***d electron configuration***	**Ionic radius[1] (Å)**	**Electronegativity[2]**	***pK_a***[3,4]	***Hydration enthalpy (kJ mol^{-1})***[5,6]
Mn^{2+}	d^5	0.83	1.263	10.8	-2743
Fe^{3+}	d^5	0.645	1.556	2.19	-5764
Co^{2+}	d^7	0.745	1.321	9.65	-2904
Ni^{2+}	d^8	0.69	1.367	9.86	-2986
Cu^{2+}	d^9	0.73	1.372	8	-2989
Zn^{2+}	d^{10}	0.74	1.336	8.86	-2936

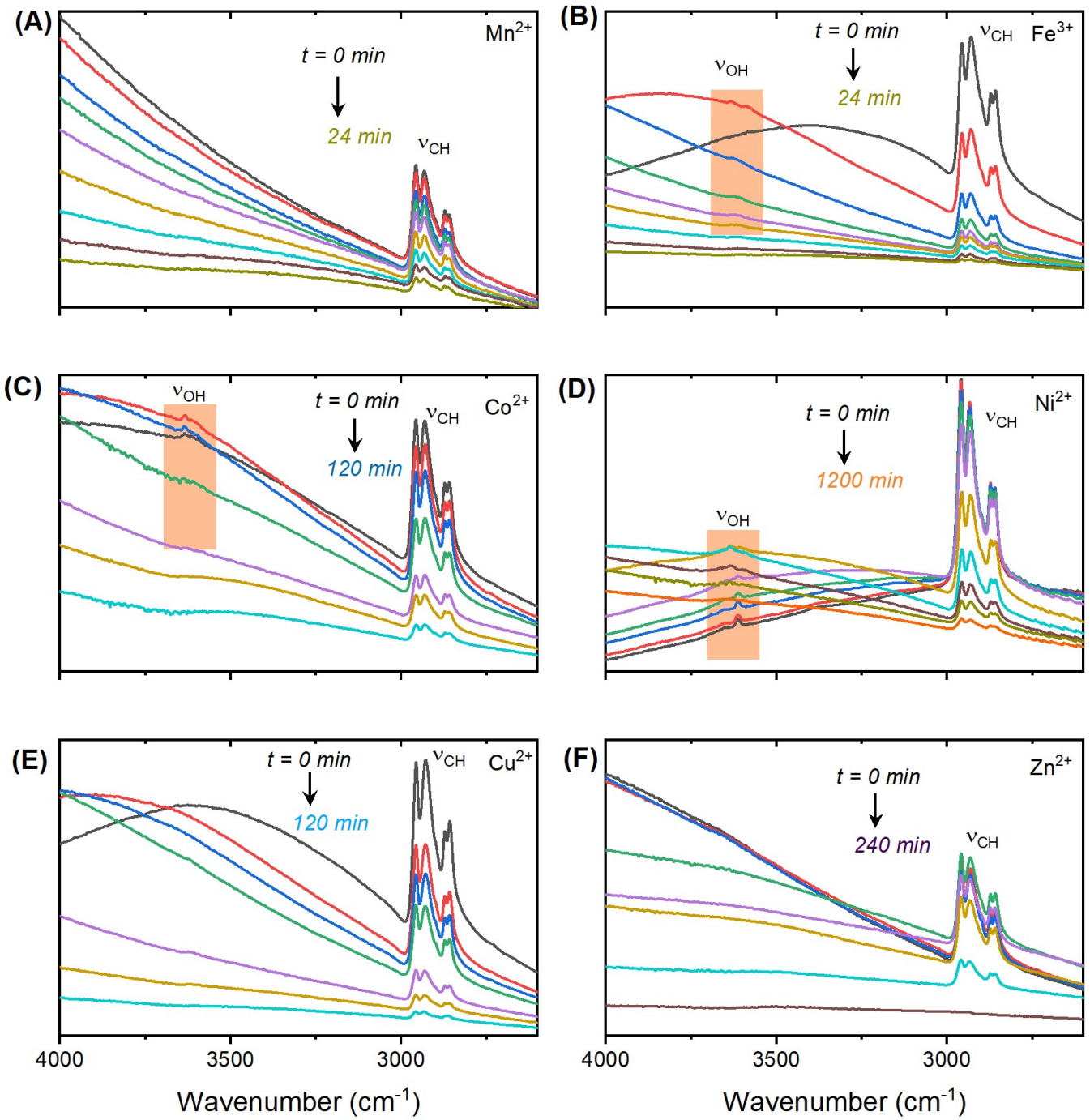

Figure S1. IR spectra of precursor films at different photolysis time. **(A)** Mn(II) 2-ethylhexanoate, **(B)** Fe(III) 2-ethylhexanoate, **(C)** Co(II) 2-ethylhexanoate, **(D)** Ni(II) 2-ethylhexanoate, **(E)** Cu(II) 2-ethylhexanoate, and **(F)** Zn(II) 2-ethylhexanoate.

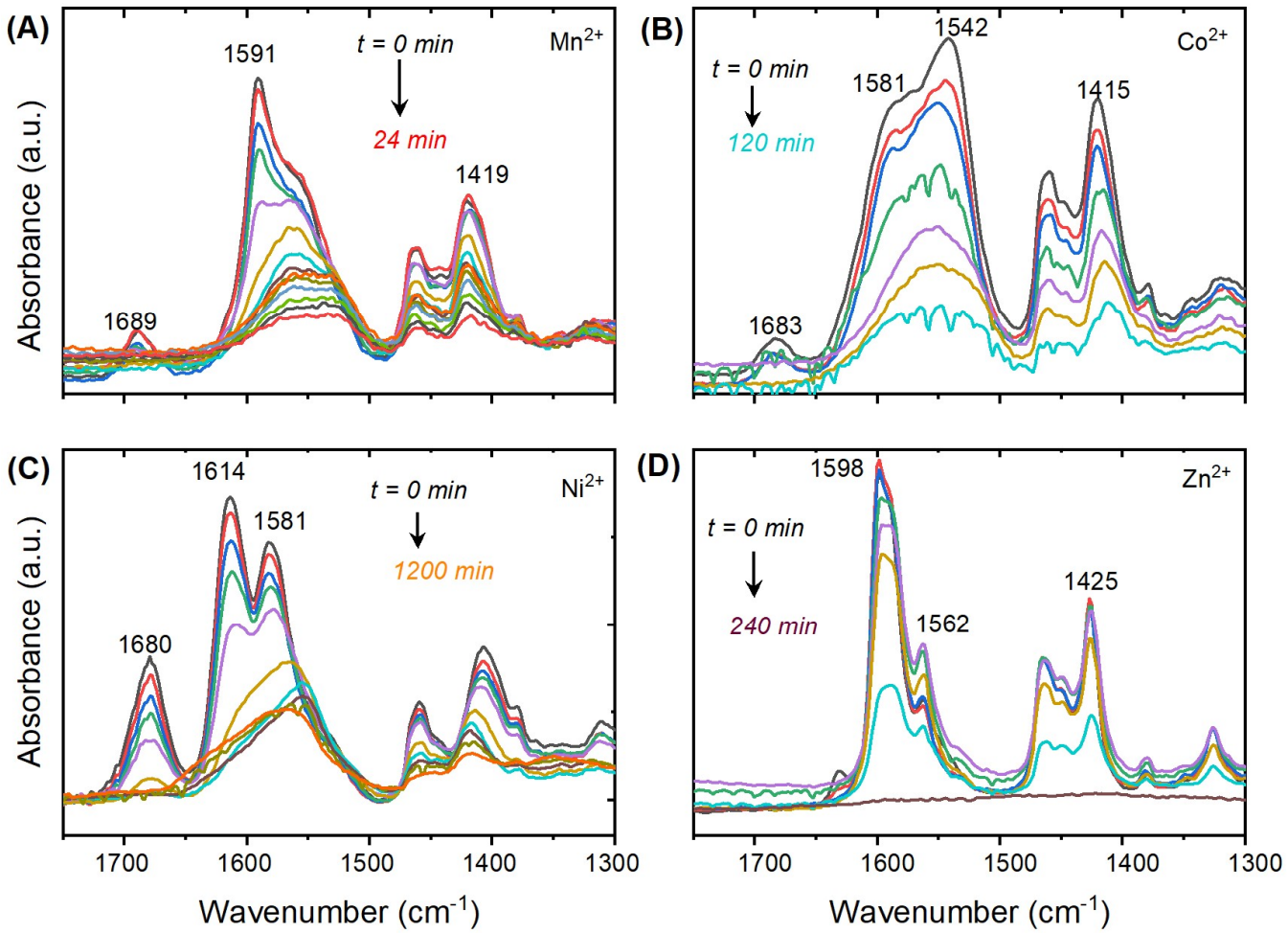

Figure S2. IR spectra of monometallic precursor films at different photolysis time. **(A)** Mn(II) 2-ethylhexanoate, **(B)** Co(II) 2-ethylhexanoate, **(C)** Ni(II) 2-ethylhexanoate, and **(D)** Zn(II) 2-ethylhexanoate.

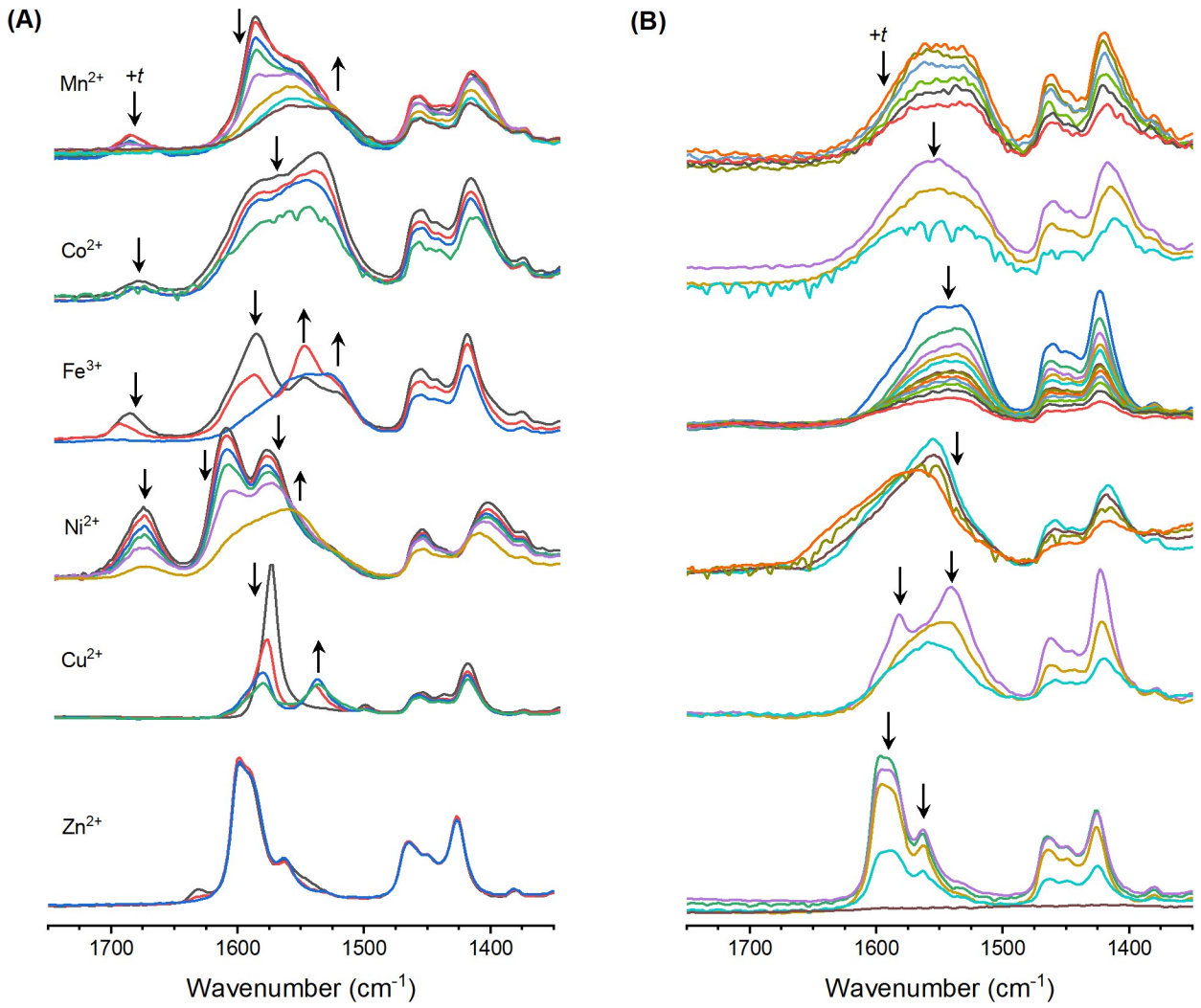

Figure S3. FTIR spectra of monometallic transition metal 2-ethylhexanoate precursor films separated into the **(A)** first and **(B)** second stages of decay.

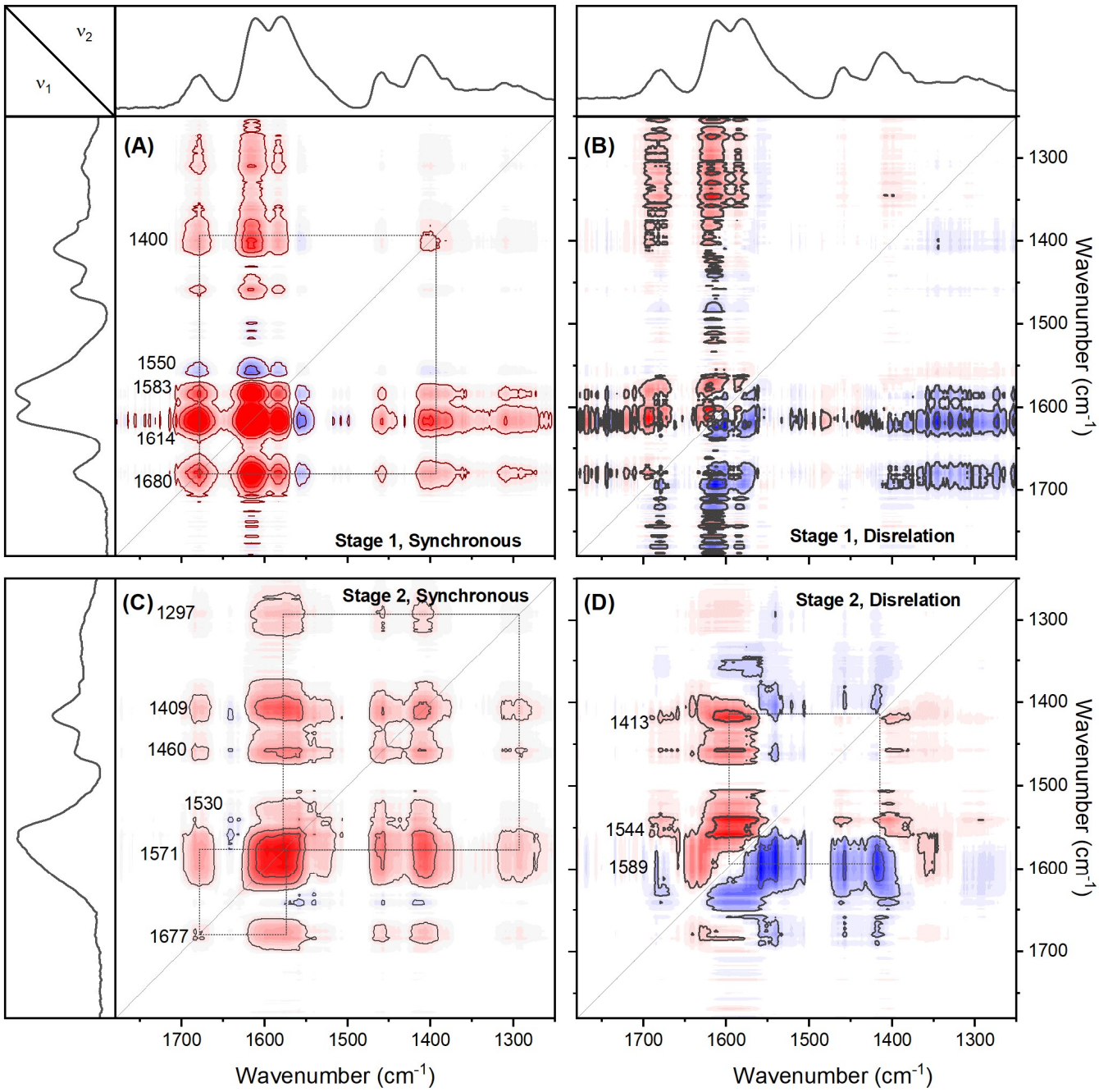

Figure S4. Two-dimensional IR correlation spectra for photochemically induced decomposition of nickel(II) 2-ethylhexanoate precursor films. **(A)** Synchronous and **(B)** disrelation plots in the first stage of decomposition. **(C)** Synchronous and **(D)** disrelation plots in the second stage of decomposition.

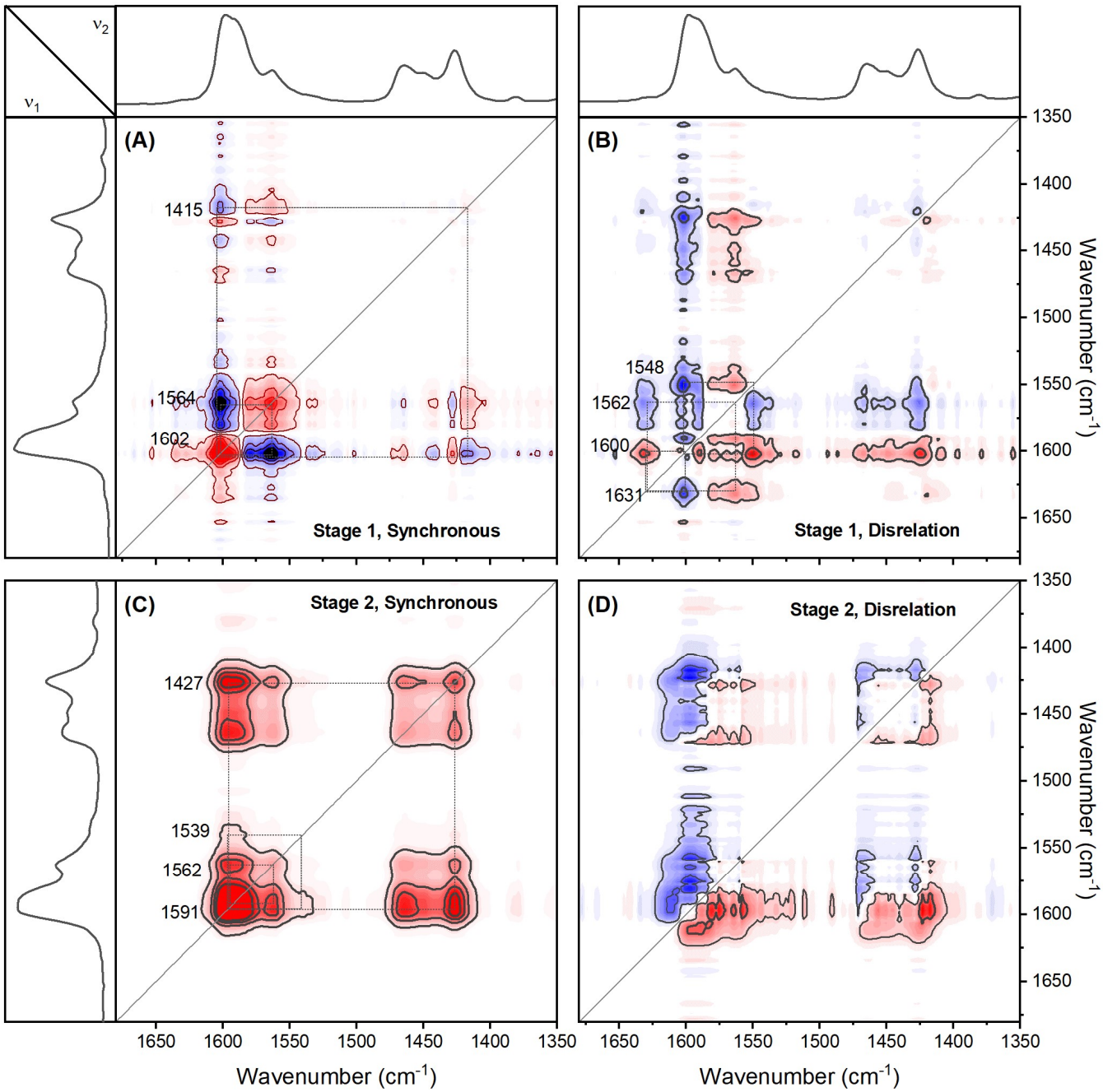

Figure S5. Two-dimensional IR correlation spectra for photochemically induced decomposition of zinc(II) 2-ethylhexanoate precursor films. **(A)** Synchronous and **(B)** disrelation plots in the first stage of decomposition. **(C)** Synchronous and **(D)** disrelation plots in the second stage of decomposition.

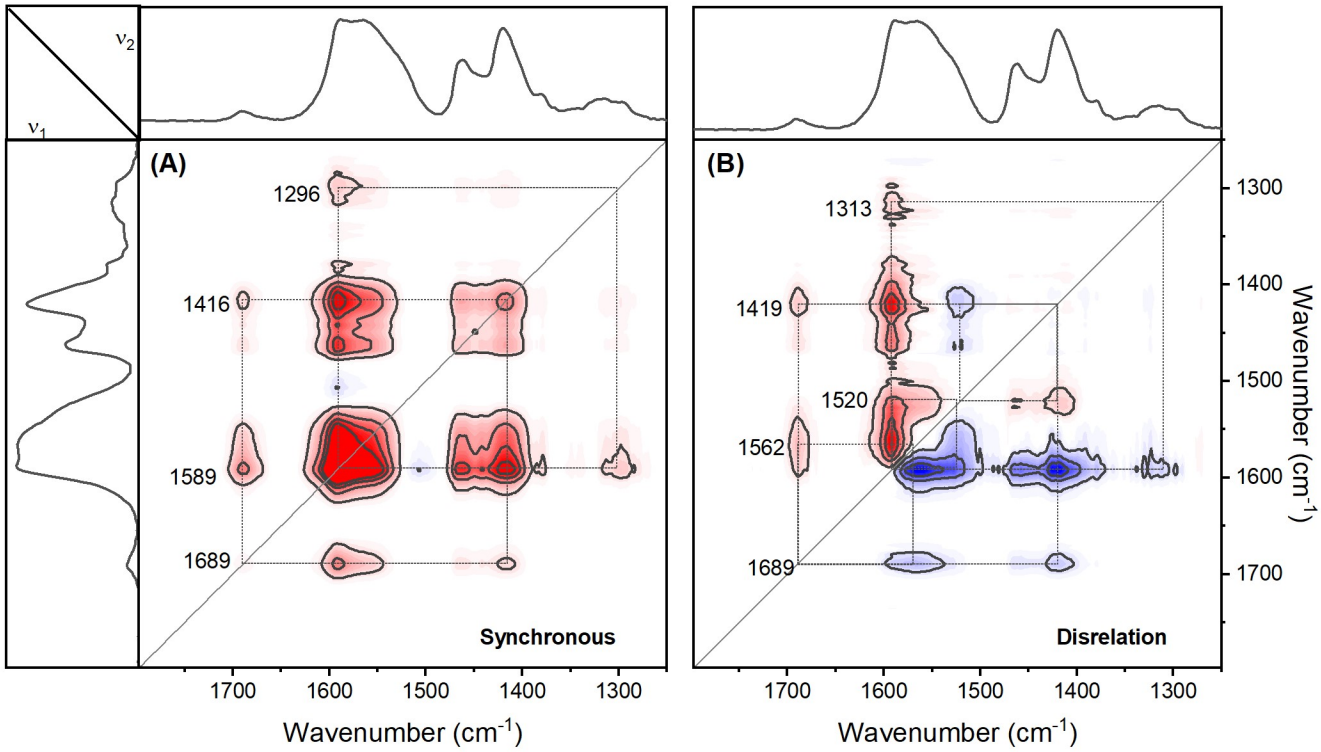

Figure S6. Two-dimensional IR correlation spectra for photochemically induced decomposition of manganese(II) 2-ethylhexanoate precursor films. **(A)** Synchronous and **(B)** disrelation plots of decomposition.

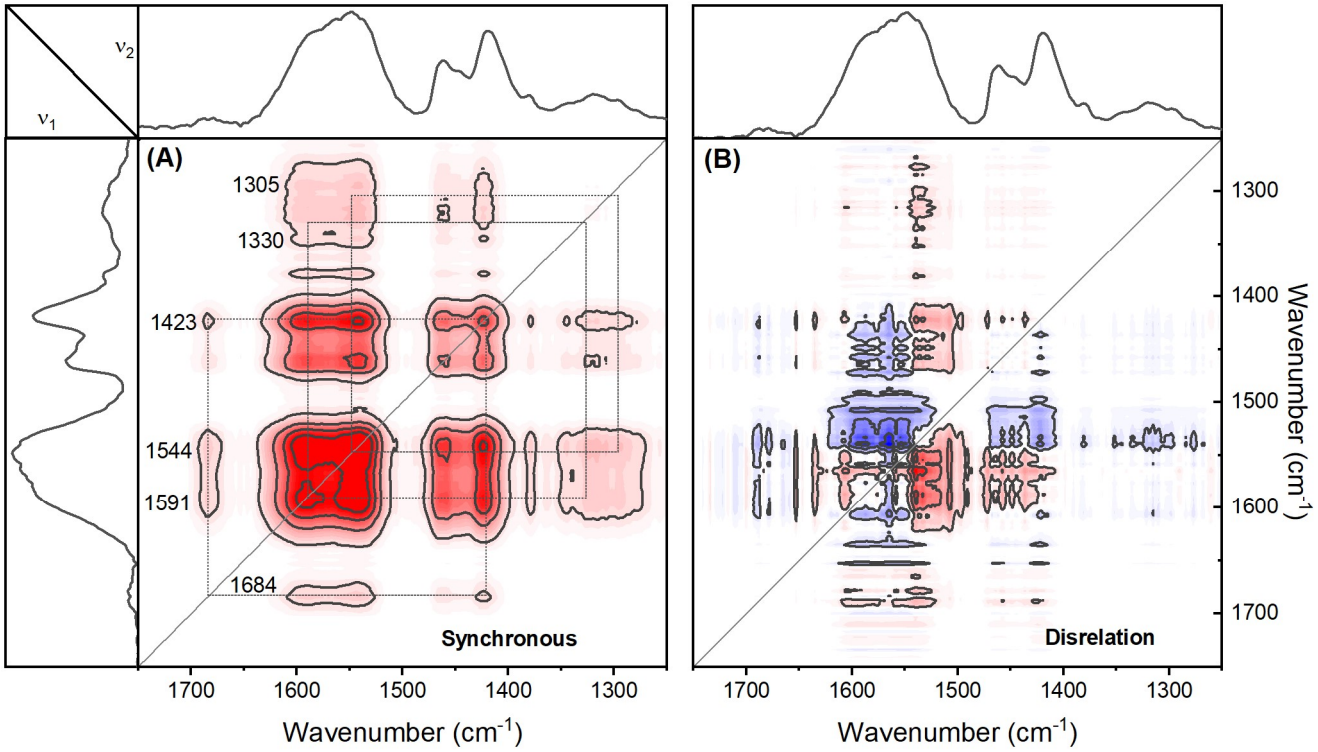

Figure S7. Two-dimensional IR correlation spectra for photochemically induced decomposition of cobalt(II) 2-ethylhexanoate precursor films. **(A)** Synchronous and **(B)** disrelation plots of decomposition.

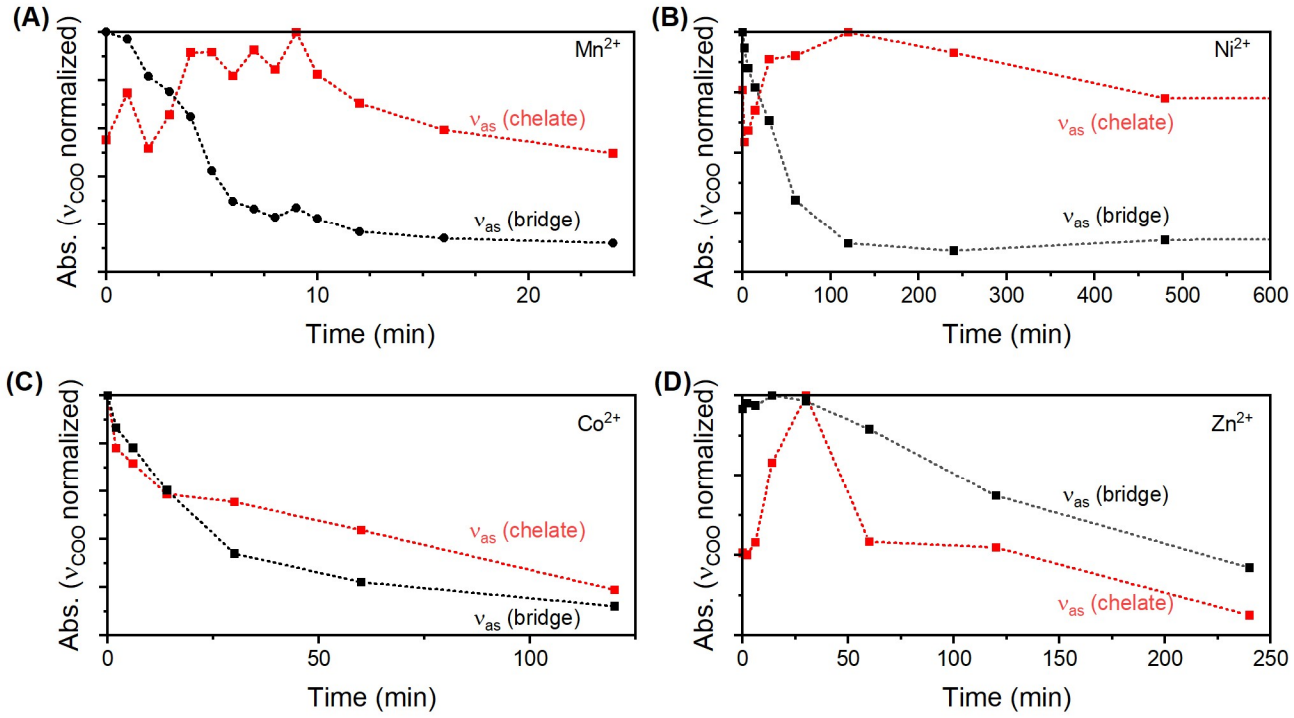

Figure S8. Chelate and bride bidentate motifs changes in photolysis of **(A)** Mn(II), **(B)** Ni(II) **(C)** Co(II), and **(D)** Zn(II) 2-ethylhexanoate precursor films.

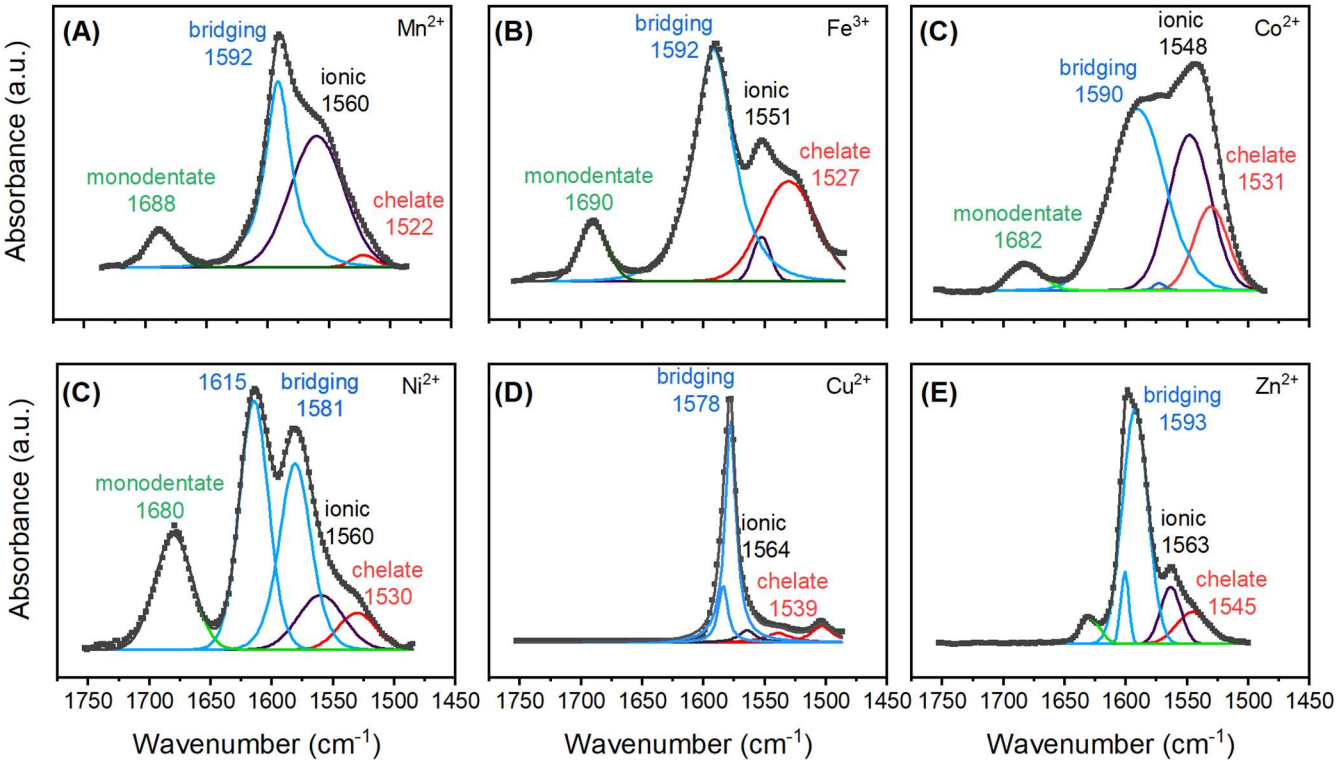

Figure S9. Asymmetric COO stretching regions of IR spectra for metal 2-ethylhexanoate precursor films at t = 0 min (before photolysis). Data shown for **(A)** Mn(II), **(B)** Fe(III), **(C)** Co(II), **(D)** Ni(II), **(E)** Cu(II), and **(F)** Zn(II) 2-ethylhexanoate.

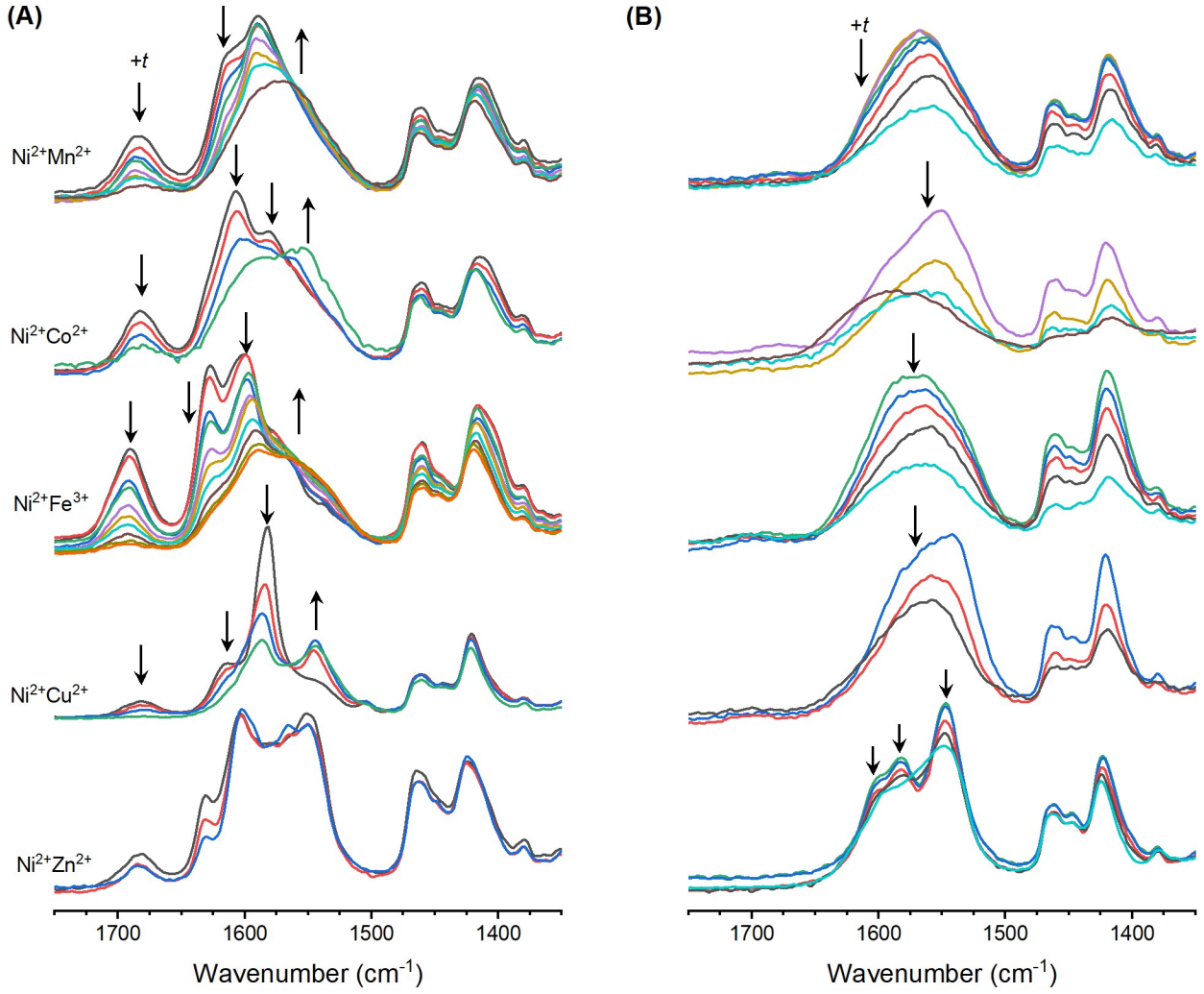

Figure S10. FTIR spectra of various bimetallic transition metal 2-ethylhexanoate precursor films separated into the **(A)** first and **(B)** second stages of decay.

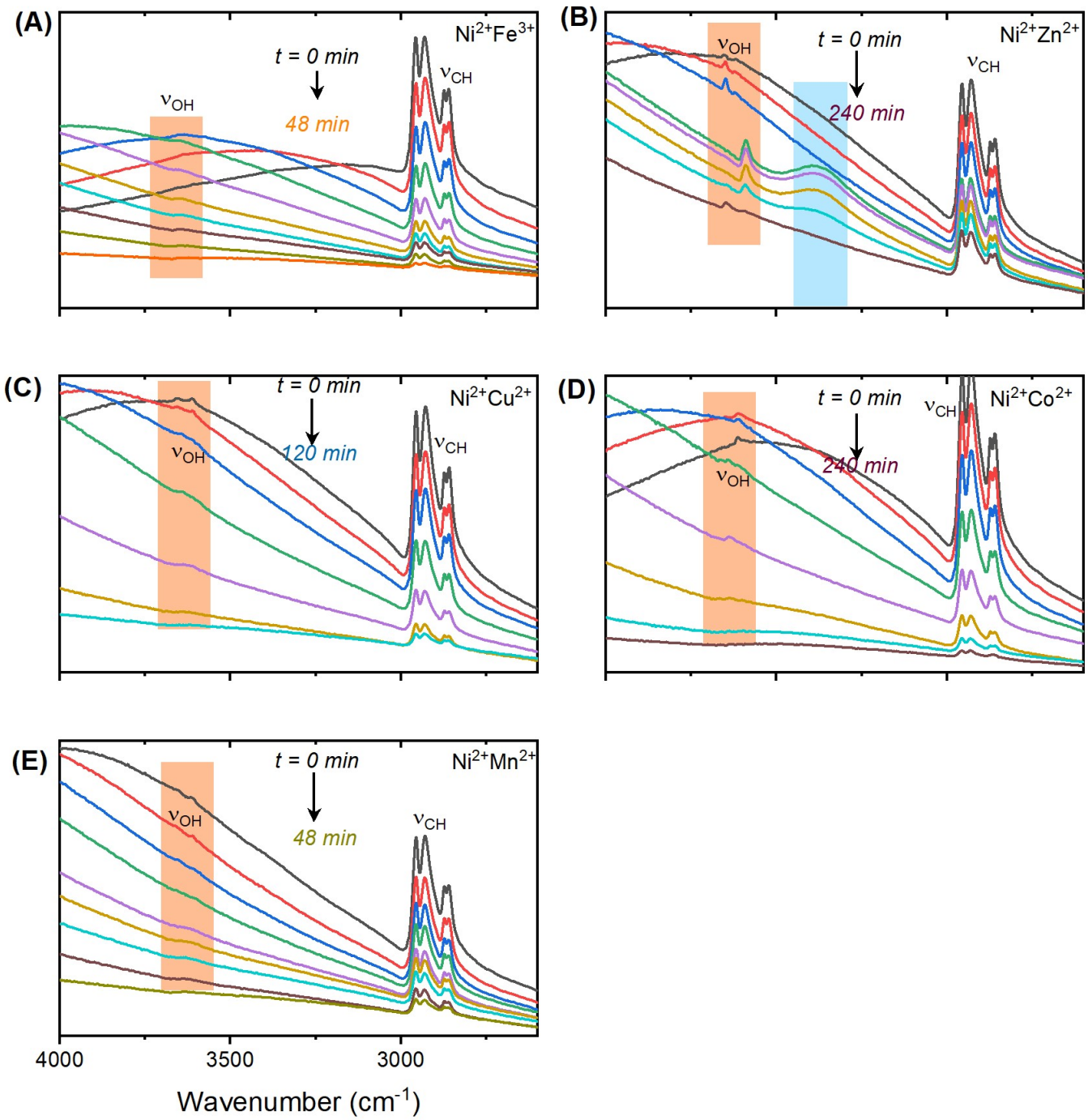

Figure S11. IR spectra of precursor films at different photolysis time. **(A)** Ni(II)Fe(III) 2-ethylhexanoate, **(B)** Ni(II)Zn(II) 2-ethylhexanoate, **(C)** Ni(II)Cu(II) 2-ethylhexanoate, **(D)** Ni(II)Co(II) 2-ethylhexanoate, and **(E)** Ni(II)Mn(II) 2-ethylhexanoate.

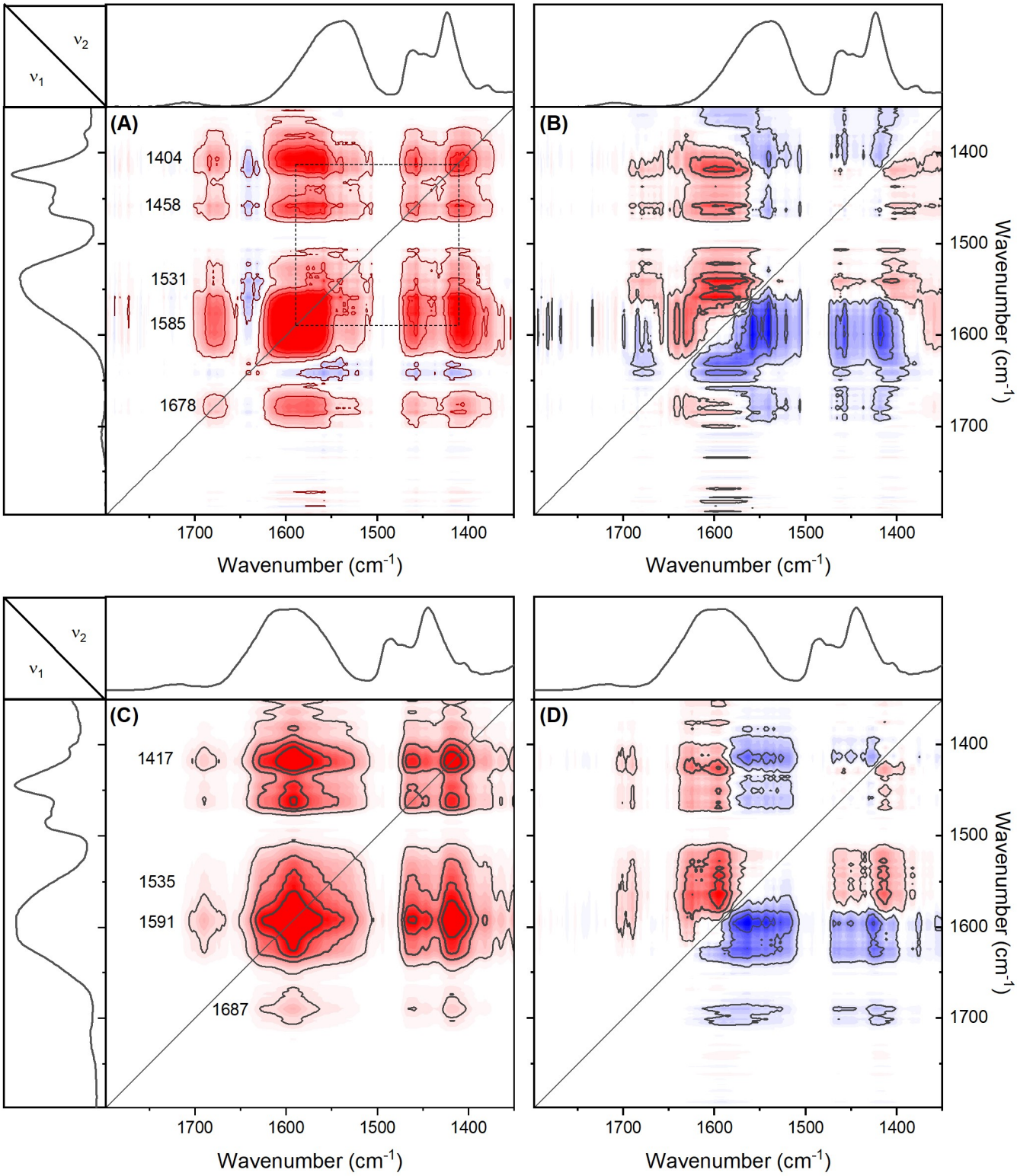

Figure S12. Comparison of two-dimensional correlation spectroscopy for photochemically induced decomposition of a pure Ni(II) film with a 1:1 mixture of Fe(III) and Ni(II). **(A)** Synchronous and **(B)** disrelation plots in the second stage of decomposition of the Ni sample. **(C)** Synchronous and **(D)** disrelation plots in the second stage of decomposition for the Fe-Ni sample.

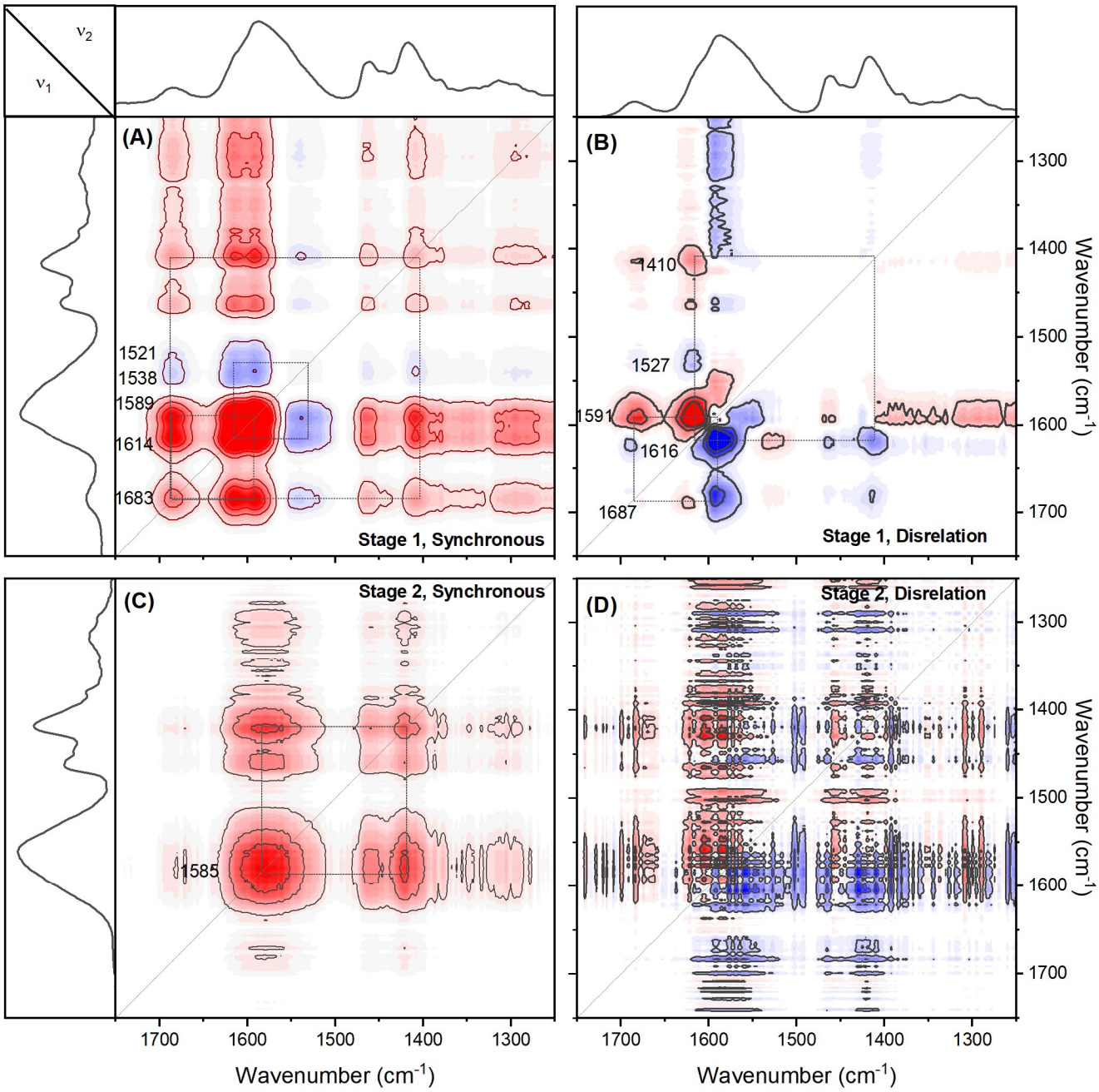

Figure S13. Two-dimensional IR correlation spectra for photochemically induced decomposition of Ni(II)Mn(II) 2-ethylhexanoate precursor films. **(A)** Synchronous and **(B)** disrelation plots in the first stage of decomposition. **(C)** Synchronous and **(D)** disrelation plots in the second stage of decomposition.

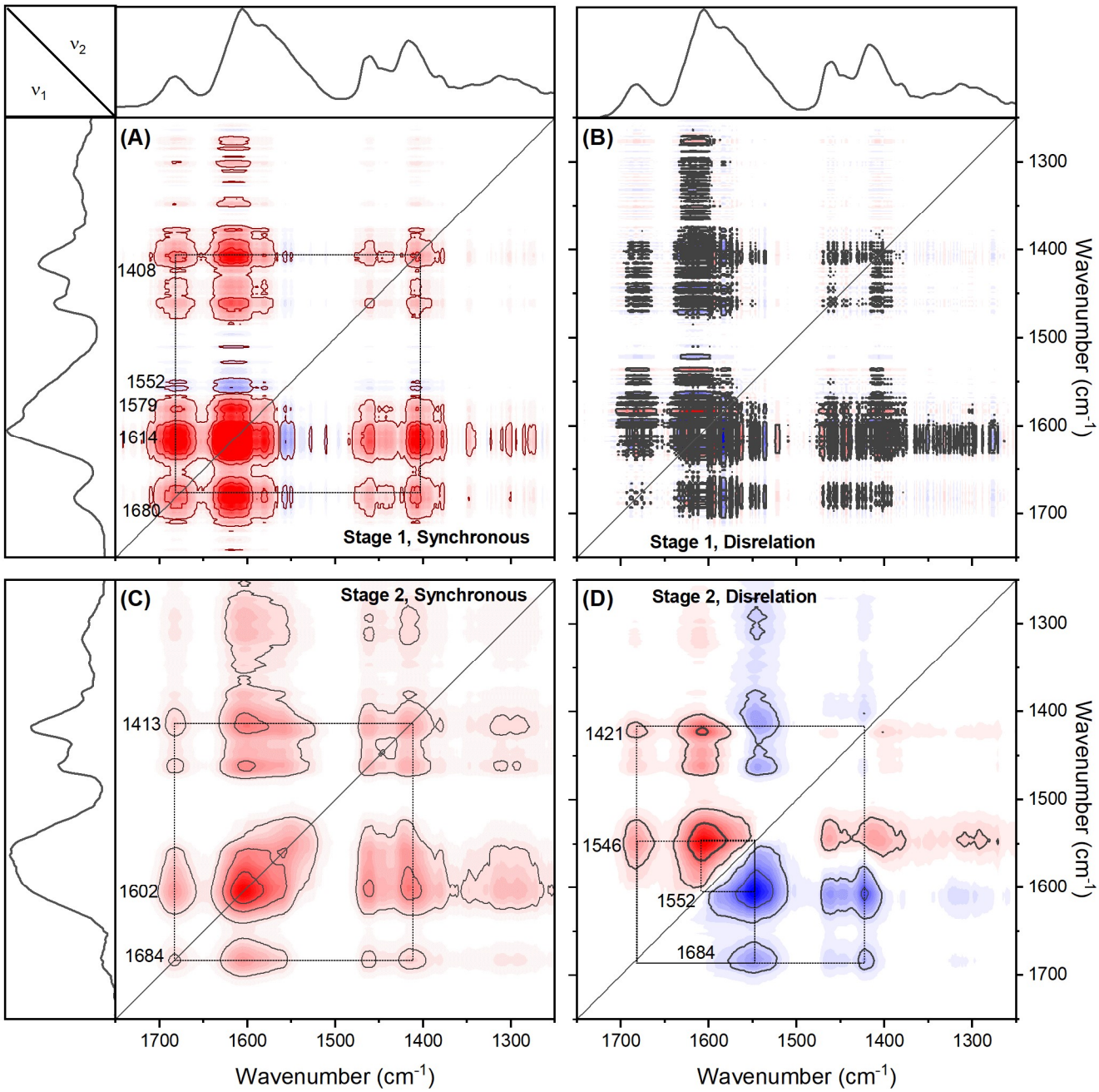

Figure S14. Two-dimensional IR correlation spectra for photochemically induced decomposition of Ni(II)Co(II) 2-ethylhexanoate precursor films. **(A)** Synchronous and **(B)** disrelation plots in the first stage of decomposition. **(C)** Synchronous and **(D)** disrelation plots in the second stage of decomposition.

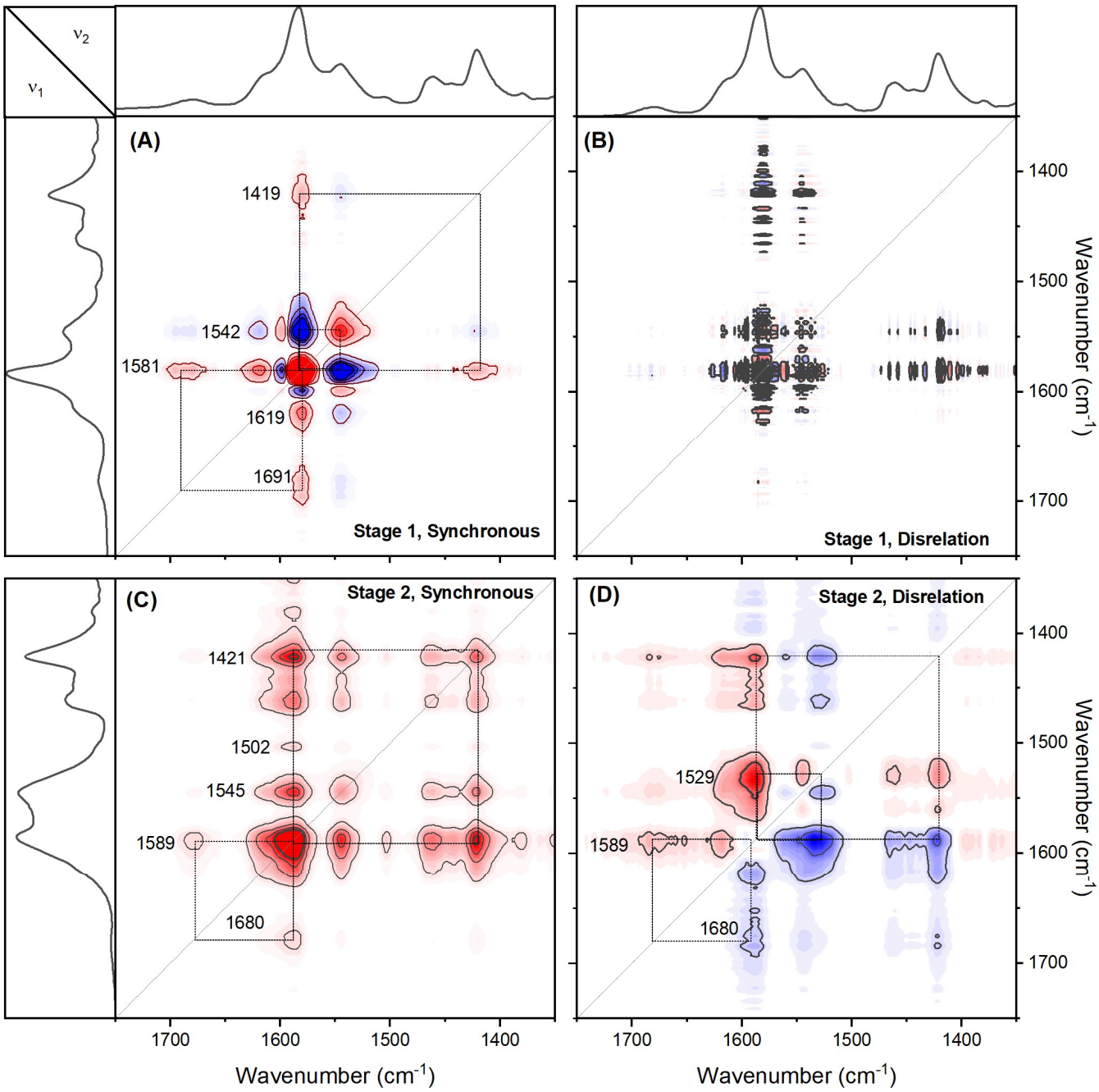

Figure S15. Two-dimensional IR correlation spectra for photochemically induced decomposition of Ni(II)Cu(II) 2-ethylhexanoate precursor films. **(A)** Synchronous and **(B)** disrelation plots in the first stage of decomposition. **(C)** Synchronous and **(D)** disrelation plots in the second stage of decomposition.

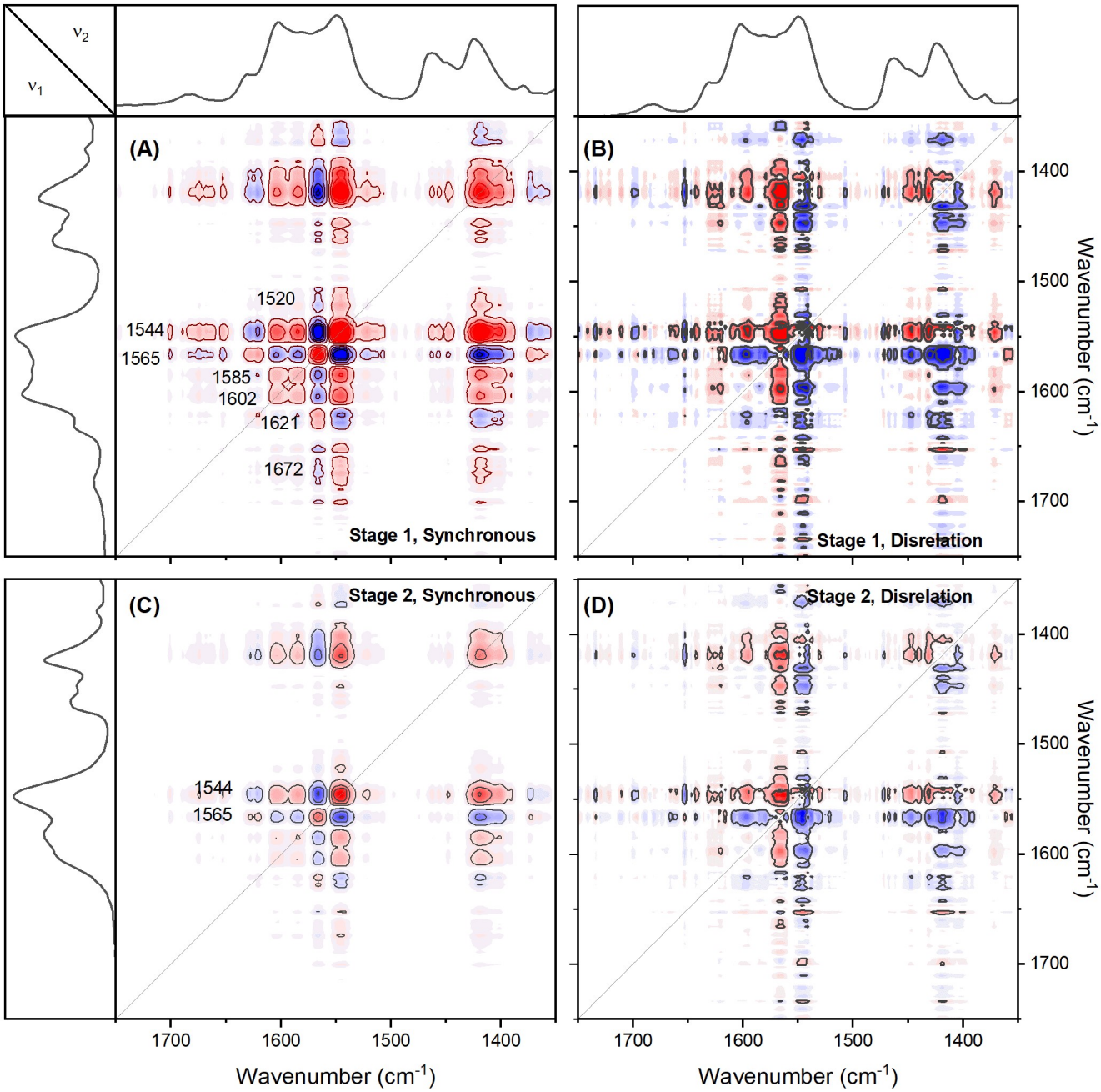

Figure S16. Two-dimensional IR correlation spectra for photochemically induced decomposition of Ni(II)Zn(II) 2-ethylhexanoate precursor films. **(A)** Synchronous and **(B)** disrelation plots in the first stage of decomposition. **(C)** Synchronous and **(D)** disrelation plots in the second stage of decomposition.

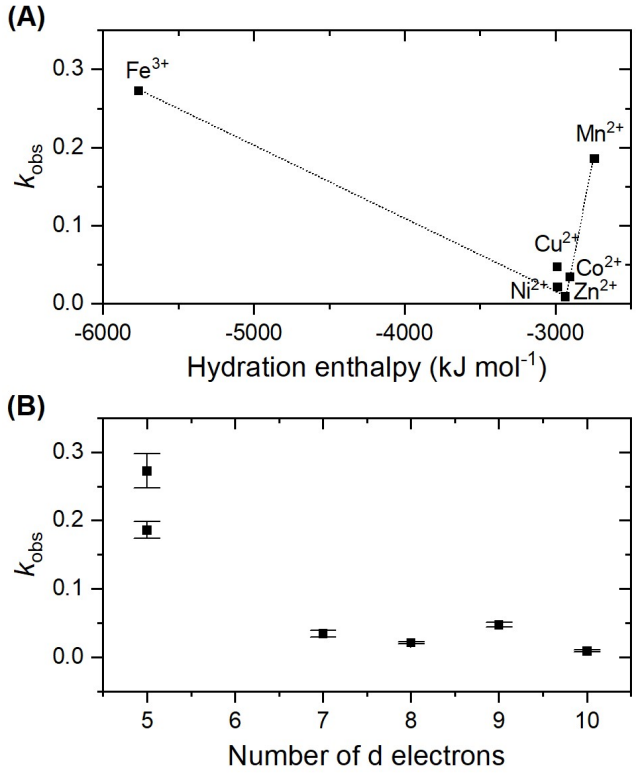

Figure S17. The observed rate constant plotted against **(A)** hydration enthalpy of metal ions and **(B)** the number of *d* electrons in the transition metal ions.

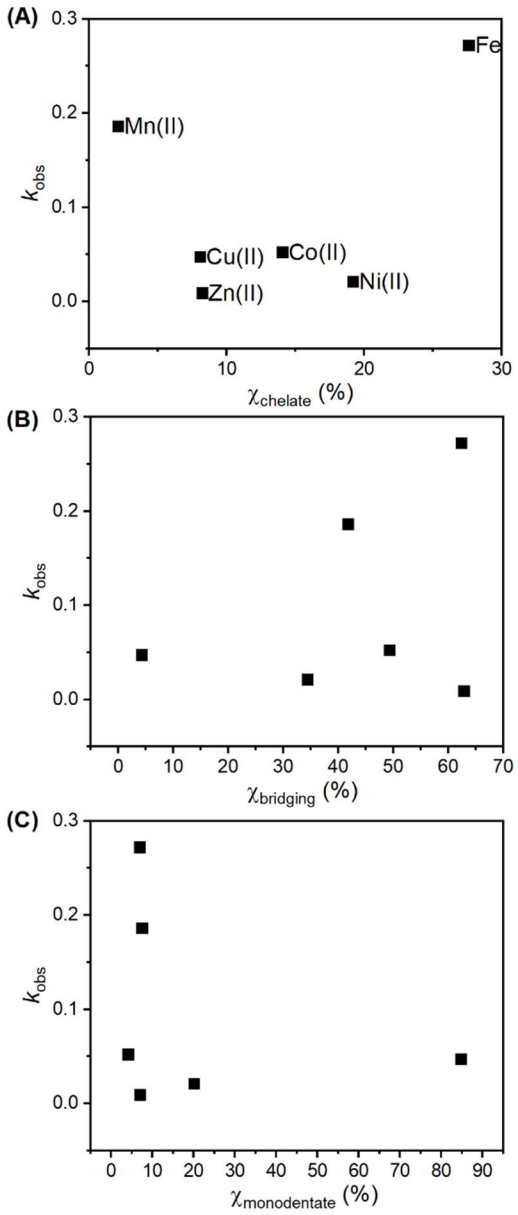

Figure S18. The observed rate constant plotted against the relative percentage of ligands bound in a **(A)** chelating, **(B)** bridging, and **(C)** monodentate fashion.

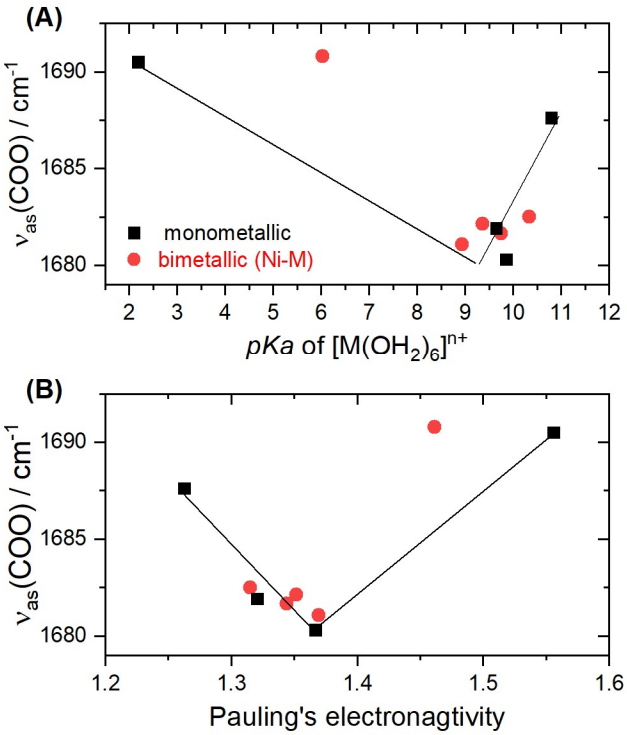

Figure S19. Correlation plot of **(A)** $\nu_{as}(COO)_{monodentate}$ versus pK_a of aqua metal ion and **(B)** $\nu_{as}(COO)_{monodentate}$ versus Pauling's electronegativity.

References

(1) Shannon, R. D. Revised Effective Ionic Radii and Systematic Studies of Interatomic Distances in Halides and Chalcogenides. *Acta Crystallogr. Sect. A* **1976**, *32* (5), 751–767. https://doi.org/10.1107/S0567739476001551.

(2) Li, K.; Xue, D. Estimation of Electronegativity Values of Elements in Different Valence States. *J. Phys. Chem. A* **2006**, *110* (39), 11332–11337. https://doi.org/10.1021/jp062886k.

(3) Gilson, R.; Durrant, M. C. Estimation of the PK_a Values of Water Ligands in Transition Metal Complexes Using Density Functional Theory with Polarized Continuum Model Solvent Corrections. *Dalt. Trans.* **2009**, No. 46, 10223–10230. https://doi.org/10.1039/B911593E.

(4) Galstyan, G.; Knapp, E.-W. Computing PK_A Values of Hexa-Aqua Transition Metal Complexes. *J. Comput. Chem.* **2015**, *36* (2), 69–78. https://doi.org/10.1002/jcc.23764.

(5) Johnson, D. A.; Nelson, P. G. Factors Determining the Ligand Field Stabilization Energies of the Hexaaqua 2+ Complexes of the First Transition Series and the Irving-Williams Order. *Inorg. Chem.* **1995**, *34* (22), 5666–5671. https://doi.org/10.1021/ic00126a041.

(6) Johnson, D. A.; Nelson, P. G. Ligand Field Stabilization Energies of the Hexaaqua 3+ Complexes of the First Transition Series. *Inorg. Chem.* **1999**, *38* (22), 4949–4955. https://doi.org/10.1021/ic990426i.